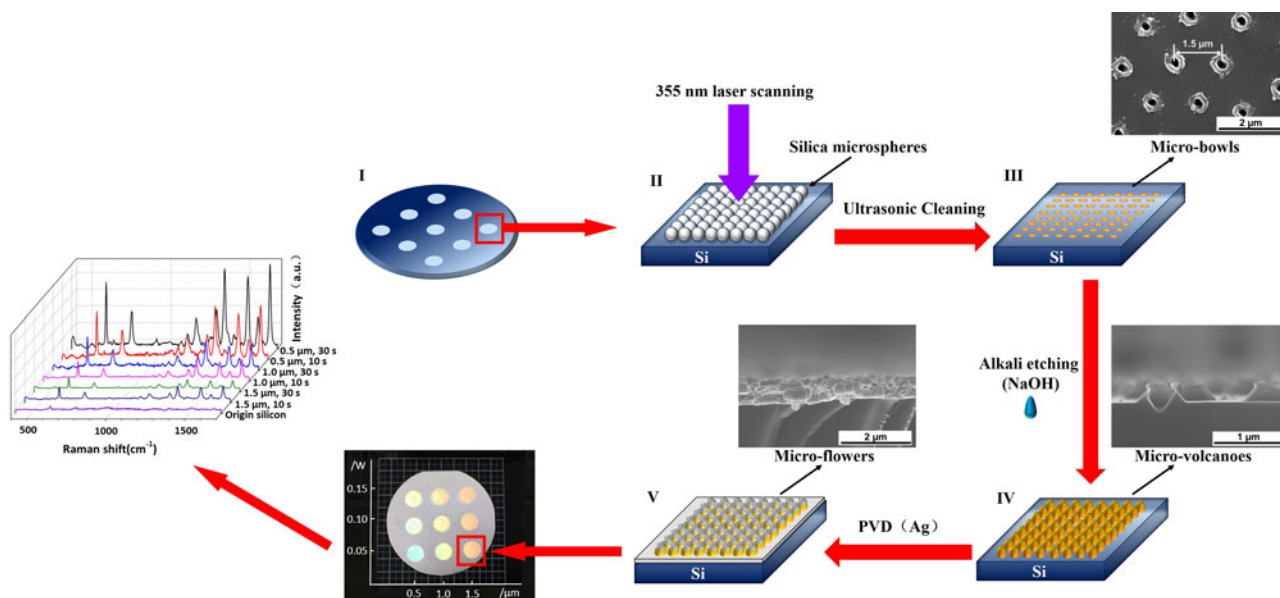


# Laser Microsphere Lens Array Fabrication of Micro/Nanostructures with Tunable Enhanced SERS Behavior in Dipole Superposition Plasmon Mode

Volume 9, Number 4, August 2017

Zhenyuan Lin  
Lingfei Ji  
Lin Li  
Jie Liu  
Yan Wu  
Meiling Zheng



DOI: 10.1109/JPHOT.2017.2715343  
1943-0655 © 2017 IEEE

# Laser Microsphere Lens Array Fabrication of Micro/Nanostructures with Tunable Enhanced SERS Behavior in Dipole Superposition Plasmon Mode

Zhenyuan Lin,<sup>1</sup> Lingfei Ji,<sup>1</sup> Lin Li,<sup>2,1</sup> Jie Liu,<sup>3</sup> Yan Wu,<sup>1</sup>  
and Meiling Zheng<sup>3</sup>

<sup>1</sup>Institute of Laser Engineering, Beijing University of Technology, Beijing 100124, China

<sup>2</sup>School of Mechanical, Aerospace and Civil Engineering, University of Manchester, Manchester M13 9PL, U.K.

<sup>3</sup>Laboratory of Organic NanoPhotonics and CAS Key Laboratory of Bio-Inspired Materials and Interfacial Science, Technical Institute of Physics and Chemistry, Chinese Academy of Sciences, Beijing 100190, China

DOI:10.1109/JPHOT.2017.2715343

1943-0655 © 2017 IEEE. Translations and content mining are permitted for academic research only.

Personal use is also permitted, but republication/redistribution requires IEEE permission.

See [http://www.ieee.org/publications\\_standards/publications/rights/index.html](http://www.ieee.org/publications_standards/publications/rights/index.html) for more information.

Manuscript received May 2, 2017; revised June 9, 2017; accepted June 10, 2017. Date of publication June 30, 2017; date of current version August 8, 2017. This work was supported by the National Natural Science Foundation of China under Grants 51575013 and 51275011. Corresponding author: Lingfei Ji (ncltji@bjut.edu.cn).

**Abstract:** Silicon-based surface-enhanced Raman scattering (SERS) substrates with high sensitivity and uniformity were obtained by a laser surface processing method utilizing microsphere lens arrays followed by chemical etching and silver (Ag) deposition. High SERS performance of these substrates was demonstrated by their enhancement factor of up to  $8.2 \times 10^7$  for rhodamine 6G (R6G) as well as their ability to detect 1 nM of R6G and 10 ppm of fenthion by a rapid drop-evaporation detection method. A dipole superposition plasmon mode due to a novel Ag microflower structures formed on the top of microvolcano microstructures fabricated before Ag deposition was found to be responsible for the SERS enhancement. The height of the Ag microflowers was not determined by Ag deposition thickness but by the height of the microvolcanoes, which could be easily tuned by laser power, microsphere size, and alkali etching time; tunable SERS performance was also achieved. The developed approach provides a cost-effective way to prepare large-area 3-D solid SERS substrates to adapt to multiple species of probe molecules and different excitation wavelength ranges with high controllability and reproducibility.

**Index Terms:** Ultrafast lasers, Raman spectroscopy, silicon nanophotonics.

## 1. Introduction

The combination of the Raman scattering, SERS based on the excitation of localized surface plasmon resonance (LSPR) has been used to enhance Raman signal intensity to detect very low concentrations of analyte species, even at the single-molecule detection level [1]–[3]. Ag, Au, and Cu particles less than 100 nm in size are the main applications for SERS active substrates because of their intrinsic electronic configuration, which can lead to LSPR around them [4]–[6]. The LSPR of the metal nanoparticles strongly depends on their size, shape, and environment as well as composition [7]. To date, designing and controlled fabrication of diverse forms of distributed metal particles

have been and continue to attract extensive attention with the aim of enhancing the intensity of homogeneous, stable SERS signals by orders of magnitude. To extend SERS applications to wider fields with more convenience, three-dimensional (3D) SERS nanostructures have been proposed because a multidimensional structure on a substrate can support more hotspots and target analytes with increased surface areas [8]. Besides, 3D nanostructures can avoid the aggregation of the particles during SERS applications, which is a common issue with nanoscale building blocks [9].

Preferred interest in processing 3D SERS solid substrates by micro/nano surface patterning is growing. This approach has been proposed to overcome the instability, inhomogeneity, and low reproducibility of chemical synthesis from aqueous solvents [10]–[15]. Electron-beam lithography, focused ion beam, and deep-ultraviolet lithography are the reported techniques to achieve high precision and reproducibility on the fabrication of nanoscale surface structures [16]–[23]. However, these techniques require expensive equipment and acute environments, such as vacuum or auxiliary gas, which make them costly and time-consuming. In addition, these methods do not readily lend themselves to scale up of electromagnetic field enhancement for SERS applications.

Laser processing has been demonstrated as a simple route with high flexibility to form micro/nanostructures that can be conducted under ambient conditions. Several groups reported fabrication of SERS substrates with favorable performance consisting of 2D/quasi-3D nanoparticle structures by laser processing [7], [20], [24]–[27]. In these studies, one strategy was laser ablation of metals in aqueous media [28]. Oxidation of metal nanomaterials could be minimized using this technique, but wet ablation routes possess common problems such as instability and reproducibility. Thus, it is worth exploring alternative solutions to preparing solid SERS substrates with high sensitivity, uniformity, and stability by taking advantage of laser surface processing methods.

In this research, 3D silicon-based SERS substrates fabricated in air were decorated with Ag. The specific surfaces created exhibited excellent performance with very high enhancement factors (EFs) of rhodamine 6G (R6G) of up to  $8.2 \times 10^7$  and high sensitivity with a lowest measurable concentration of 1 nM. The substrates were fabricated with a chemical-assisted laser surface processing method combined with Ag deposition. By guiding laser irradiation onto self-assembled dielectric microsphere arrays, submicron structures with a new crystal orientation and low surface free energy were obtained. In our study, laser scanning irradiation through dielectric microspheres were used to obtain periodic patterns on silicon surface with high fabrication efficiency and high controllability which was demonstrated by many investigators [29]–[35]. Subsequent alkali etching for  $\leq 30$  s based on the anisotropic etching effects of Si resulted in the formation of 3D microvolcano arrays. Through Ag deposition, 3D microflower morphologies were formed at the position of the volcano-like microstructures. Supported by finite-difference time-domain (FDTD) simulation analysis, the high uniformity and sensitivity of SERS behavior exhibited by the substrates was found to originate from local electromagnetic fields in dipole superposition plasmon mode. Tunable SERS performance was achieved by changing the dimensions and spacing of the 3D microstructure arrays. The features of the fabricated microstructures were readily controlled by laser power, microsphere diameter, and alkali etching time, which can be modulated to realize selective patterning of the surface microstructure. The developed approach is a facile, controllable surface patterning strategy to produce 3D silicon-based SERS substrates with thousands or millions of ordered 3D submicron structures to enable highly uniform and sensitive SERS analysis of multiple species of probe molecules.

## 2. Experimental Fabrication

A schematic illustration of the process developed to fabricate SERS substrates involving multiple steps of chemical-assisted laser fabrication followed by Ag deposition is depicted in Fig. 1. Silicon samples covered with self-assembled transparent dielectric microsphere monolayer arrays were exposed to irradiation from an Edgewave 355-nm picosecond (ps) laser with a 10-ps pulse width at room temperature under atmospheric conditions. The microspheres were silica in size of 0.5, 1, or 1.5  $\mu\text{m}$ . The microsphere aqueous solution with a calculated concentration was prepared and directly spread on the silicon. The substrate was kept on in an airtight space and placed at

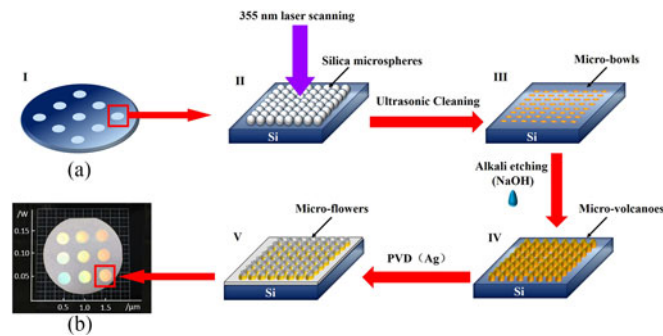


Fig. 1. (a) Schematic illustration of the 3D SERS substrate fabrication process: I) self-assembled microsphere array on a silicon surface, II) laser scanning irradiation, III) micropit structures obtained after ultrasonic cleaning, IV) microvolcano structures formed after alkali etching, and V) microflower structures produced by Ag decoration. (b) Photograph of nine SERS substrates fabricated using different parameters on a silicon wafer. The horizontal and vertical axes are the microsphere size and laser power, respectively.

small angle ( $10^\circ$ ) to ensure the high uniformity of monolayer microsphere arrays. To keep the incident laser homogeneous in the fabricated area, the laser beam was set to scanning mode with a  $20\text{-}\mu\text{m}$  line interval because the size of the laser spot was  $25\ \mu\text{m}$  in Gaussian distribution. The laser scanning speed was  $1200\ \text{mm/s}$ , pulse repetition rate was  $200\ \text{kHz}$ , and laser power ranged from  $0.05\ \text{W}$  to  $0.15\ \text{W}$ . The laser was incident vertically to the samples. The frequency and the time of ultrasonic cleaning were  $40\ \text{kHz}$  and  $5\ \text{min}$ , respectively.

After ultrasonic cleaning to remove the residual microspheres, the laser-treated samples were then processed in NaOH solution by means of the anisotropic etching property of silicon. In the alkali etching step, The NaOH solution was previously heated to  $75\ \text{degree Centigrade}$  and the etching time was from  $10$  to  $30\ \text{s}$ . Both the NaOH and alcohol concentrations were maintained at  $10\ \text{wt. \%}$ . The etched substrate was dealt with  $10\ \text{min}$  ultrasonic cleaning in deionized water. The etched samples were coated with Ag by physical vapor deposition (PVD). The PVD process was completed in vacuum within  $10\ \text{min}$  by a magnetron sputtering system. The Ag target used in PVD was  $99.99\%$  pure. Fig. 1(b) shows nine SERS substrates with an  $8\text{-mm}$  diameter fabricated on a  $2\text{-inch}$  silicon wafer using different processing parameters.

### 3. Results and Discussion

Obtaining of micro/nanostructures on silicon or metal substrates by laser irradiation of self-assembled transparent dielectric microsphere arrays were reported in many investigations [34]–[37]. Here, we used this method to not only controllably fabricate microstructures with a micropit shape that depended on the near-field modulation of the dielectric microsphere, but also particularly emphasize to intentionally induce local changes of crystal orientation around the fabricated structures. Unlike most previous studies, which used a UV excimer laser or IR- or visible-wavelength ultrashort laser [33], [35], [38], [39], we employed a  $355\text{-nm}$  ps laser to provide ultra-short pulse width and short wavelength to enable the formation of micropits with precise location, size, and features, which is the key point for the subsequent processing.

Scanning electron microscopy (SEM) images of the micropit structure arrays fabricated from microsphere of different diameter ( $0.5$ ,  $1$ , and  $1.5\ \mu\text{m}$ ) (Fig. 2(a)–(c)) revealed that the spacing between micropit centers was equal to the diameter of the microspheres. In addition, the width and depth of the micropit structures also correlated well with the microsphere diameter because of their near-field optical enhancement effect. Thus, the location and dimensions of the micropit structures can be regulated by the diameter of the close-packed microspheres under the same laser power.

By fixing the laser power at  $0.15\ \text{W}$ , the burr on the edge of the micropits became more and more obvious with increasing microsphere diameter. Correspondingly, a visible ring bulge surrounding the bowls was induced by the microspheres with the largest diameter of  $1.5\ \mu\text{m}$

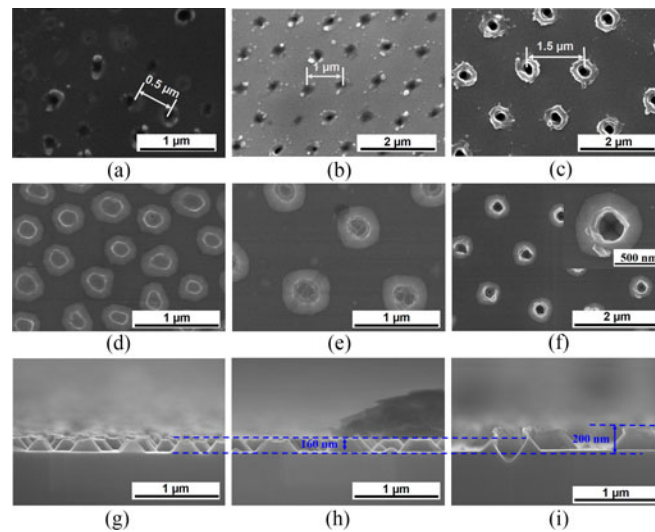


Fig. 2. SEM images of micropit arrays formed by laser irradiation of a silicon substrate covered with microspheres of different diameter: (a)  $0.5\ \mu\text{m}$ , (b)  $1\ \mu\text{m}$ , and (c)  $1.5\ \mu\text{m}$ . (d), (e), and (f) SEM images of microvolcanoes formed by alkali etching the surfaces in (a), (b), and (c), respectively, for 30 s. (g), (h), (i) Cross-sectional SEM images of microvolcano arrays corresponding to (d), (e), and (f), respectively.

TABLE 1

Parameters of Microvolcanoes Fabricated Using a Laser Power of 0.15 W, Microspheres of Different Size, and Subsequent Etching for 30 s

Microsphere diameter ( $\mu\text{m}$ )	0.5	1	1.5
FWHM (nm)	$325 \pm 25$	$450 \pm 25$	$550 \pm 25$
Height (nm)	$160 \pm 10$	$160 \pm 10$	$200 \pm 20$

(Fig. 2(c)). Fig. 2(d), (e), and (f) show the morphologies of the microstructures obtained following 30 s of alkali etching of the micropit microstructures corresponding to those shown in Fig. 2(a), (b), and (c), respectively. After alkali etching, the laser-treated micropit structures changed to bump-shaped structures with volcano-like features, which became more pronounced with increasing microsphere diameter at the same laser power and etching time. On the top of each microvolcano, the bowl-shaped micropatterns with different depths still remained. The dimensions of the microvolcanoes were restricted to the area of the burr region found in the samples shown in Fig. 2(a)–(c). Table 1 summarizes the full width at half-maximum (FWHM) and height of the microvolcanoes determined from the images in Fig. 2.

During the chemical etching process, the burr region resulting from ps laser irradiation acted as a self-mask to limit the etching lateral dimension. Different etching rate occurred between the burr region and spaces among the micropits under the same laser irradiation and etching conditions. It is this etching rate difference between the two regions that caused the microvolcano structures to form. The cross-sectional SEM images of the microvolcanoes obtained from 0.5- and  $1\text{-}\mu\text{m}$  microspheres (Fig. 2(g) and (h), respectively) showed they were the same height of about 160 nm. This demonstrates that the etching rate of the space regions on the different surfaces was the

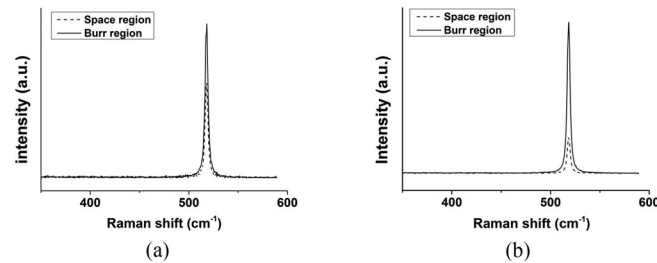


Fig. 3. Micro Raman spectra measured in the space and burr regions (a) before alkali etching, and (b) after alkali etching.

same. Extra height about of 40 nm exists on the microvolcanoes formed from the 1.5- $\mu\text{m}$  microspheres (Fig. 2(i)) which originated from the ring bulge present before alkali etching of this surface (see Fig. 2(c)).

Anisotropic etching of silicon occurs because of the different etching rates of its different crystal orientations. This means that there were different crystal orientations in the burr region and space region of the samples. The micro Raman spectra of these samples shown in Fig. 3 all contained a typical Si peak at  $518\text{ cm}^{-1}$ , which indicates that there was no phase change from crystalline to amorphous or residual stress or oxidation on the sample surfaces. However, the Raman intensity of the burr region in samples both before and after alkali etching was obviously enhanced compared with that in the space region. Furthermore, the signal enhancement after alkali etching was several times larger than that before etching. Such peak intensity variation indicates that the preferred crystal orientation in the two regions is different, even though there are no phase changes in the materials.

The average Raman peak intensity of silicon with (111) crystal orientation is larger than that of silicon with (100) crystal orientation [40]. In the experiments, (100) Si wafers were used. The enhanced local optical field induced by laser irradiation of the microspheres caused resolidification of the silicon substrate, which resulted in the formation of the burr around the micropit structure. Resolidification can be associated with confined recrystallization in which the growth rate of crystal faces depends on surface atomic density. According to the Bravais rule, the growth of the (100) orientation is the slowest because it possesses the smallest surface atomic density; the (111) orientation forms more easily [41]. Thus, after resolidification, the (111) crystal orientation and other crystal orientations deviating from (100) were dominant in the burr region, while the (100) orientation still remained in the space region. The variation of the peak intensity of silicon in Fig. 3(a) reflects the different crystal orientations in the two different regions. During chemical etching, the burr region with deviated crystal orientation from (100) had a slower etching rate than that of the space region with (100) orientation because of its low surface free energy, so it acted as an etch-stop layer remained on the silicon wafer. Correspondingly, as shown in Fig. 3(b), more exposure of crystal orientation deviating from (100) during etching was revealed by the further enhancement of the peak intensity after etching.

Table 2 lists the FWHM of the microvolcanoes fabricated using 0.5- $\mu\text{m}$  microspheres with different etching time and laser power. The higher the laser power and longer the etching time, the larger the FWHM of the microstructures. Based on the above results, it is concluded that the morphology of microvolcanoes can be readily tuned by modulating the microsphere diameter, laser power, and etching time. To obtain a larger bump structure, higher laser power, larger microsphere diameter, and longer etching time are necessary.

After Ag deposition, 3D flower-like architectures with overall dimensions of hundreds of nanometers were obtained on the silicon substrates. Fig. 4(a), (b), and (c) are typical SEM images of the 3D microflowers with a 160 nm-thick Ag coating originating from the microvolcanoes obtained from 0.5-, 1-, and 1.5- $\mu\text{m}$  microspheres, respectively, using a laser power of 0.15 W and etching time of 30 s. The original structure features of the microvolcanoes (e.g., height, width, and space

TABLE 2  
Parameters of Microvolcanoes Fabricated Using 0.5- $\mu\text{m}$  Microspheres With Different Etching Time and Laser Power

Laser power (W)	0.05		0.1		0.15	
Etching time (s)	10	30	10	30	10	30
FWHM (nm)	$120 \pm 20$	$180 \pm 20$	$150 \pm 30$	$250 \pm 30$	$200 \pm 20$	$325 \pm 25$

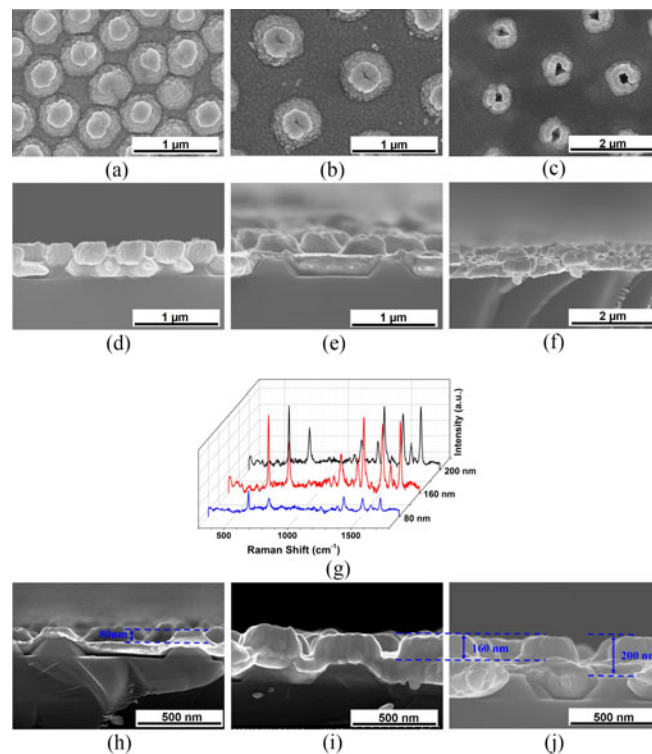


Fig. 4. SEM images of Ag-decorated microflower arrays obtained from microvolcanoes with different spacing of (a) 0.5  $\mu\text{m}$ , (b) 1  $\mu\text{m}$ , and (c) 1.5  $\mu\text{m}$ . (d), (e), and (f) Cross-sectional images corresponding to the structures in (a), (b), and (c), respectively. (g) SERS spectra of silicon substrates corresponding to samples with Ag coatings of different thickness; the x-axis indicates the Ag coating thickness. Cross-sectional SEM images of microflower arrays with Ag coatings with thicknesses of (h) 80 nm, (i) 160 nm, and (j) 200 nm.

region width) were maintained after Ag deposition. The corresponding cross-sectional images in Fig. 4(d)–(f) reveal that the microflowers are not the microvolcanoes covered with an Ag coating but novel structures formed from the Ag nanoparticles acting as nanoscale building blocks on the top of the microvolcanoes. The space between the microvolcanoes was also filled up with a continuous, uniform coating of Ag. The SERS behavior of samples fabricated using 0.5- $\mu\text{m}$  microspheres, 0.15-W laser power, and 30-s etching time with different Ag coating thicknesses of 80, 160, and 200 nm are illustrated in Fig. 4(g). For the SERS measurements, R6G solution with concentrations

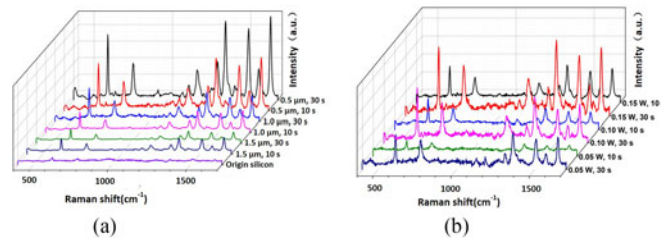


Fig. 5. SERS spectra of R6G molecules measured on various substrates. (a) Silicon substrates with microflower arrays fabricated by 0.15-W laser irradiation using different etching times and microsphere diameters. Microsphere size and etching time are indicated on the y-axis. (b) Silicon substrates with microflower arrays fabricated by laser irradiation of 0.5- $\mu\text{m}$  microspheres with different etching time and laser power. (Laser power and etching time are indicated on the y-axis).

1  $\mu\text{M}$  and 20  $\mu\text{L}$  volumes in deionized water was drop-evaporated in air on the fabricated substrates for tests. To pursue rapid-detection, all SERS measurements were carried out by the short-time drop-evaporation method. The SERS response of the samples increased with the thickness of the Ag coating from 80 to 160 nm, but showed moderate change as the Ag thickness was increased from 160 to 200 nm. Fig. 4(h)–(j) indicates that the heights of the 3D Ag microflowers in the samples with 160 and 200 nm-thick Ag coatings are the same. This is attributed to the synchronous Ag deposition on the microvolcanoes and the spaces between them. The spaces between microvolcanoes would be filled up with Ag coating when the deposition thickness reached the microvolcano height, which is about 160 nm in our study. Further Ag deposition would not change the height of the 3D Ag nano-architectures because of the synchronous increase of Ag coating thickness, so the SERS behavior did not intensify any more. The Ag deposition thickness is not directly responsible for the SERS signal enhancement, but it supports the height of the 3D Ag nanoarchitectures, which depends on the height of the microvolcanoes produced by the process of laser irradiation and chemical etching. Once the microvolcano height is decided, the height of the 3D Ag nanoarchitectures that can tune the SERS enhancement effect is determined.

Typical SERS spectra of the original (100) silicon substrate with a 160-nm Ag coating and samples fabricated using different laser powers, microsphere diameters, and etching time (including the samples shown in Fig. 4(a)–(j)) are presented in Fig. 5. For the SERS measurements, an aqueous solution of R6G (10 mM) was prepared. This solution concentration was diluted down to 1 nM for SERS quantitative analysis. About 20  $\mu\text{L}$  of the solution was added dropwise onto the surface of the samples for measurements. SERS performance was measured by a laser with an excitation wavelength of 532 nm and power of 0.5 mW. Compared with those of the original silicon substrate with an Ag coating, enhanced R6G Raman intensities of all characteristic peaks at 614, 774, 1183, 1310, 1363, 1509, 1572, and 1650  $\text{cm}^{-1}$  can be clearly distinguished on all of the fabricated 3D microflower substrates. The 3D substrates fabricated using a 0.15-W laser power, 0.5- $\mu\text{m}$  dielectric microspheres, and 30 s of alkali etching showed the maximum Raman signal enhancement, which is approximately  $10^4$  times that of the Ag-decorated original substrate. At the same laser power and etching time, the enhancement of the SERS intensities increases as the microsphere diameter decreases (Fig. 5(a)). Fig. 5(b) shows the change of Raman spectra with the laser power and etching time used to fabricate the SERS substrates. Increasing laser power and etching time also obviously increase the SERS signal. In accordance with the analysis of the results in Fig. 4, these findings confirm that the SERS performance of the microflower substrates is controlled by the microsphere diameter, laser power, etching time, and height of the 3D Ag nanoarchitectures.

The uniformity of SERS signals of the 3D flower-like Ag-coated substrates was verified by Raman mapping of R6G molecules at the 614  $\text{cm}^{-1}$  peak. Five different Raman mapping images of  $10 \times 10 \mu\text{m}$  areas distributed over different locations on the SERS substrate presented in Fig. 6(a) and the corresponding average SERS spectra shown in Fig. 6(b) exhibit good large-scale uniformity

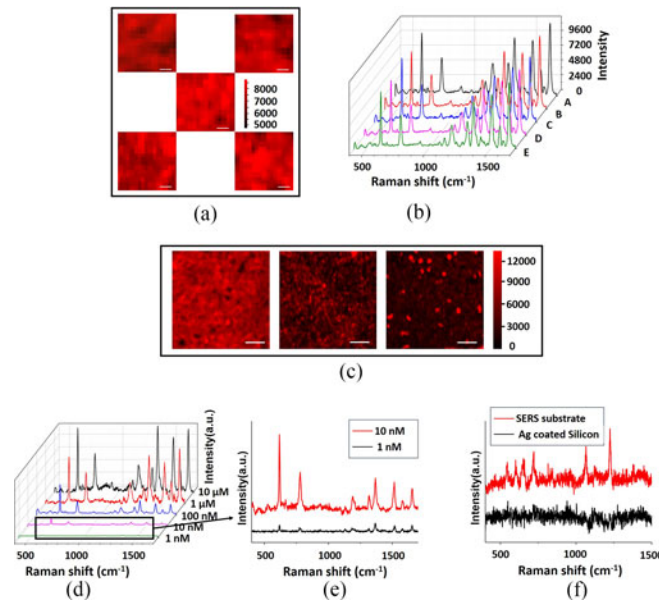


Fig. 6. (a) Raman mapping images of R6G molecules at  $614\text{ cm}^{-1}$  at five different  $10 \times 10\ \mu\text{m}$  areas on a 3D microflower SERS substrate fabricated using  $0.15\text{-W}$  laser irradiation,  $0.5\text{-}\mu\text{m}$  microspheres, and an etching time of  $30\text{ s}$ . The scale bar is  $2\ \mu\text{m}$ . (b) Average SERS spectra for the five areas in (a). (c) Raman mapping images at  $614\text{ cm}^{-1}$  of  $50 \times 50\ \mu\text{m}$  areas on the SERS substrate fabricated using  $0.15\text{-W}$  laser irradiation, an etching time of  $30\text{ s}$ , and  $0.5\text{-}$ ,  $1\text{-}$ , and  $1.5\text{-}\mu\text{m}$  microspheres (from left to right). The scale bar is  $10\ \mu\text{m}$ . (d) SERS spectra of various concentrations of R6G molecules on the 3D substrates. The y-axis indicates the concentration of R6G. (e) Magnified image of the corresponding view in (d). (f) Raman spectra of fenthion on a 3D SERS substrate and Ag-coated silicon substrate.

with less than 7% deviation from the signal at  $614\text{ cm}^{-1}$ . The uniform SERS signals are attributed to the high periodicity and homogeneity of the microflower arrays. Fig. 6(c) displays Raman mapping of the  $614\text{ cm}^{-1}$  peak over  $50 \times 50\ \mu\text{m}$  areas on three kinds of 3D microflower substrates fabricated using microsphere sizes of  $0.5$ ,  $1$ , and  $1.5\ \mu\text{m}$ . The homogeneity of the substrates increased with the diameter of the microspheres.

The sensitivity of the SERS substrates was measured using R6G solutions with different concentrations, as shown in Fig. 6(d). The SERS intensity of signal peaks gradually decreased with R6G concentration. However, the Raman peaks of R6G were clearly distinguished even when the R6G concentration was lowered to  $1\text{ nM}$  (Fig. 6(e)). The corresponding optimal SERS EF was estimated using (1) [42].

$$EF = (I_{SERS}/N_{Surf}) / (I_{RS}/N_{Vol}) \quad (1)$$

Where  $I_{SERS}$  is the SERS intensity,  $I_{RS}$  is the intensity of normal Raman measurements,  $N_{Surf}$  is the average number of R6G molecules contributing to the normal Raman scattering signal, and  $N_{Vol}$  is the average number of R6G molecules contributing to the SERS signal. In our experiment, the accumulating  $N_{Surf}$  and  $N_{Vol}$  were estimated from solution concentrations  $C_{SERS}$  and  $C_{RS}$ .  $C_{SERS}$  is the concentration of R6G solution corresponding to  $I_{SERS}$ .  $C_{RS}$  is the concentration of R6G solution that produces Raman signal  $I_{RS}$  under non-SERS conditions. The intensity of the SERS peak at  $614\text{ cm}^{-1}$  was measured under the following laser excitation conditions: acquisition time of  $1\text{ s}$  and laser power of  $0.5\text{ mW}$  for SERS and acquisition time of  $10\text{ s}$  and laser power of  $0.5\text{ mW}$  for Raman. The determined  $I_{SERS}$  and  $I_{RS}$  were  $9789.125$  and  $1.189$  counts per second, respectively, based on the average intensity from five areas. For the submicron-structured SERS substrates in our work,  $C_{SERS} = 1\ \mu\text{M}$ , and  $C_{RS} = 10\text{ mM}$ . Thus, the optimal EF is  $\sim 8.2 \times 10^7$ . Fig. 6(f) shows SERS spectra obtained for fenthion, which is a widely used insecticide, as specific target analyte

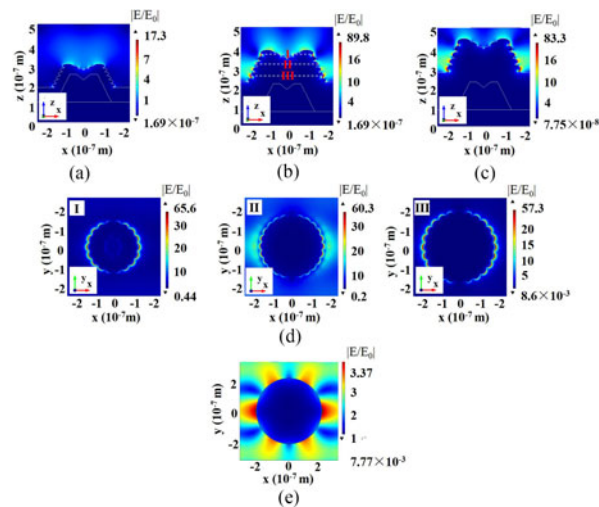


Fig. 7. FDTD simulation results of the electric field distribution corresponding to the microflowers with Ag coating thicknesses of (a) 80 nm, (b) 160 nm, and (c) 200 nm. (d) x-y view of region I, II and III indicated in (b). (e) Localized electric field distributions around 400-nm Ag nanoparticles.

in anhydrous acetonitrile solution with a concentration of 10 ppm and volume of 20  $\mu\text{L}$ , using an excitation power of 0.5 mW and relatively short acquisition time of 1 s. Distinct peaks at 1052 and 1221  $\text{cm}^{-1}$  of fenthion on the 3D SERS substrate can be obviously distinguished in the Raman spectrum while these characteristic peaks can't be observed on the Ag-coated silicon substrate. The results demonstrate that the 3D SERS substrates have strong detecting ability at nanomolar level and indicate the possibility for SERS detection at single-molecule level.

The electric field distribution of the 3D Ag microflowers fabricated using 0.5- $\mu\text{m}$  microspheres, 0.15-W laser power, and etching for 30 s was analyzed by FDTD simulation (Fig. 7(a)–(c)). Based on their observed surface morphology, the Ag nanoparticles were configured as ellipsoids with equatorial radii of  $a_{ep} = 25$  nm and  $b_{ep} = 25$  nm, and a polar radius of  $c_{ep} = 15$  nm coated on the surface of the microflowers. The heights of the microflowers were set as 80 and 160 nm, while the structure widths were decided by information deduced from the SEM images in Figs. 2 and 4. For the optical field distribution, a 532-nm beam wave was incident with x-direction polarization, which was perpendicular to the propagation direction (z-axis). Periodic boundary conditions were used to simulate the microflower arrays to reduce the calculated amount.

As shown in Fig. 7(a)–(c), Ag coatings with thicknesses of 160 and 200 nm generated larger enhancement of localized electric field distribution than that with a thickness of 80 nm. The similar distribution and value of the localized electric field enhancement models for substrates with 160- and 200-nm Ag coatings are consistent with the SERS behavior observed in Fig. 4(g). Fig. 7(d) shows three different x-y sections of electric field distribution selected along the z-direction of the microflower in Fig. 7(b). The diameters of the three sections were 200, 300, and 400 nm. It is found that the localized electric field enhancement for each section was mainly located on the outer surface of the Ag nanoarchitectures rather than in the gaps between them, which is a typical dipole resonance model [6], [43]. The polarization direction of the dipolar plasmon radiation is parallel to the polarization direction of the incident light. According to the superposition principle, the x-y section of a microflower can be considered as a combined structure consisting of the outer surface Ag nano-architectures and a large core. As shown in Fig. 7(e), the dominant direction of electron oscillations excited by the large core particle is also parallel to the polarization direction of the incident light. Electron oscillations from both the large core and outer Ag nanoarchitectures are in the same direction. In this case, the local field enhancement is confined on the surface of the core because of dipolar plasmon resonance, and further enhanced by the outer Ag nanoparticles.

Based on the equation of the radiation field induced by dipolar resonance in superposition mode [43], it has

$$E_{Total}^2 = E_0^2 + \chi_i^2 E_i^2 + 2\chi_i E_0 E_i \cos(R \cos \theta_i 2\pi/\lambda) \quad (2)$$

Where  $E_0$  and  $E_i$  are the radiation field induced by the core and outer Ag nano-architectures, respectively,  $\chi_i$  is the weighing factor,  $R$  is the size of core particle,  $\theta_i$  is the angle between a certain radiation direction of  $E_i$  and the direction perpendicular to the dipolar polarization direction. For 532-nm radiation, the overall electric field  $E_{Total} > E_0$  when the size of the core particle is less than 266 nm, which results in remarkable enhancement of the LSPR. For core sizes over 266 nm, the variation of  $E_{Total}$  depends on  $\theta_i$ . When the core diameter is 400 nm,  $E_{Total}$  is larger than  $E_0$  and  $\theta_i$  is over  $66.7^\circ$ , which is why the strongest enhancement of the localized electric field is observed in the region where  $\theta_i > 66.7^\circ$  (region III in Fig. 7(d)). Because of the superposition of dipole oscillation in the x-y sections of the microflower along the z-direction with the polarization of the incident light, the overall electric field enhancement of an entire microflower achieves practical enhancement of the local electric field in 3D space.

#### 4. Conclusion

We presented a feasible method to fabricate large-area SERS silicon substrates with controllability and reproducibility using chemical-assisted laser processing combined with Ag deposition. Following Ag deposition on the modified silicon substrates, microflowers with prominent SERS performance were obtained. The highest average EF of  $8.2 \times 10^7$  was obtained. Based on the experimental and FDTD simulation results, the enhancement of the localized electric field of the microflowers was concluded to be a dipole superposition plasmon mode in the 3D Ag microflowers which is a combined structure consisting of a core particle and outer surface coating of Ag nanoparticles, in which surface local field enhancement is mainly confined on the core particle surface and further enhanced by the Ag nanoparticle coating. The height of the microvolcanoes plays a major role in determining the overall electric field enhancement rather than the thickness of the Ag film. These results indicate that further enhancement of SERS behavior can be realized by tuning the height of surface micro/nanostructures, which offers a novel way to fabricate substrates with prominent SERS behavior to extend to multiple types of probe molecules and different excitation wavelength range.

#### Acknowledgment

The authors would like to thank Professor C. P. Pang (China Agricultural University) and postgraduate K. J. Gu (China Agricultural University) for the supply of fenthion solution.

#### References

- [1] K. Kneipp *et al.*, "Single molecule detection using surface-enhanced Raman scattering (SERS)," *Phys. Rev. Lett.*, vol. 78, pp. 1667–1670, Mar. 1997.
- [2] M. Fan *et al.*, "A review on the fabrication of substrates for surface enhanced Raman spectroscopy and their applications in analytical chemistry," *Anal. Chim. Acta*, vol. 693, pp. 7–25, Mar. 2011.
- [3] B. Sharma *et al.*, "SERS: Materials, applications, and the future," *Mater. Today*, vol. 15, pp. 16–25, Jan. 2012.
- [4] M. C. Daniel *et al.*, "Gold nanoparticles: Assembly, supramolecular chemistry, quantum-size-related properties, and applications toward biology, catalysis, and nanotechnology," *Chem. Rev.*, vol. 104, pp. 293–346, Dec. 2004.
- [5] W. A. Murray *et al.*, "Plasmonic materials," *Adv. Mater.*, vol. 19, pp. 3771–3782, Nov. 2007.
- [6] F. Zhang *et al.*, "Further localization of optical field for flower-like silver particles under laser radiation," *Laser Phys. Lett.*, vol. 10, Apr. 2013, Art. no. 045901.
- [7] K. L. Kelly *et al.*, "The optical properties of metal nanoparticles: The influence of size, shape, and dielectric environment," *J. Phys. Chem. B*, vol. 107, pp. 668–677, Jan. 2003.
- [8] R. Lu *et al.*, "A 3D-SERS substrate with high stability: Silicon nanowire arrays decorated by silver nanoparticles," *CrystEngComm*, vol. 15, pp. 6207–6212, May 2013.
- [9] M. Zhang *et al.*, "Rapid, large-scale, sonochemical synthesis of 3D nanotextured silver microflowers as highly efficient SERS substrates," *J. Mater. Chem.*, vol. 21, pp. 18817–18824, Sep. 2011.

- [10] T. Vo-Dinh, "Surface-enhanced Raman spectroscopy using metallic nanostructures," *TrAC Trends Anal. Chem.*, vol. 17, pp. 557–582, Sep. 1998.
- [11] Z. Xu *et al.*, "Nanoreplicated positive and inverted submicrometer polymer pyramid array for surface-enhanced Raman spectroscopy," *J. Nanophoton.*, vol. 5, Nov. 2011, Art. no. 053526.
- [12] J. Wang *et al.*, "An invisible template method toward gold regular arrays of nanoflowers by electrodeposition," *Langmuir*, vol. 29, pp. 3512–3517, Mar. 2013.
- [13] S. J. Pearce *et al.*, "Nanostructured surface enhanced Raman scattering sensor platform with integrated waveguide core," *Appl. Phys. Lett.*, vol. 105, Nov. 2014, Art. no. 181101.
- [14] X. F. Liu *et al.*, "Templated fabrication of periodic arrays of metallic and silicon nanorings with complex nanostructures," *Nanotechnology*, vol. 26, Feb. 2015, Art. no. 055603.
- [15] M. L. Zheng *et al.*, "Three-dimensional donut-like gold nanorings with multiple hot spots for surface-enhanced Raman spectroscopy," *Nanotechnology*, vol. 28, Jan. 2017, Art. no. 045303.
- [16] N. A. Abu Hatab *et al.*, "Surface-enhanced Raman spectroscopy substrates created via electron beam lithography and nanotransfer printing," *ACS Nano*, vol. 2, pp. 377–385, Feb. 2008.
- [17] Y. Y. Lin *et al.*, "Focused ion beam-fabricated Au micro/nanostructures used as a surface enhanced Raman scattering-active substrate for trace detection of molecules and influenza virus," *Nanotechnology*, vol. 22, Mar. 2011, Art. no. 185308.
- [18] Y. Oh *et al.*, "Glass nanopillar arrays with nanogap-rich silver nanoislands for highly intense surface enhanced Raman scattering," *Adv. Mater.*, vol. 24, pp. 2234–2237, May 2012.
- [19] Y. Chen *et al.*, "Improved SERS intensity from silver-coated black silicon by tuning surface plasmons," *Adv. Mater. Interfaces*, vol. 1, Feb. 2014, Art. no. 1300008.
- [20] J. Yang *et al.*, "Laser hybrid micro/nano-structuring of Si surfaces in air and its applications for SERS Detection," *Sci. Rep.*, vol. 4, Oct. 2014, Art. no. 6657.
- [21] Q. Zhang *et al.*, "Hierarchical 3D SERS substrates fabricated by integrating photolithographic microstructures and self-assembly of silver nanoparticles," *Small*, vol. 10, pp. 2703–2711, Jul. 2014.
- [22] Z. Hu *et al.*, "Wafer-scale double-layer stacked Au/Al<sub>2</sub>O<sub>3</sub>@Au nanosphere structure with tunable nanospacing for surface-enhanced Raman scattering," *Small*, vol. 10, pp. 3933–3942, Oct. 2014.
- [23] X. Liu *et al.*, "Tailored surface-enhanced Raman nanopillar arrays fabricated by laser-assisted replication for biomolecular detection using organic semiconductor lasers," *ACS Nano*, vol. 9, pp. 260–270, Jan. 2015.
- [24] E. D. Diebold *et al.*, "Femtosecond laser nanostructured substrates for surface-enhanced Raman scattering," *Langmuir*, vol. 25, pp. 1790–1794, Oct. 2009.
- [25] T. C. Chong *et al.*, "Laser precision engineering: From microfabrication to nanoprocessing," *Laser Photon. Rev.*, vol. 4, pp. 123–143, Jan. 2010.
- [26] M. L. Tseng *et al.*, "Fast fabrication of a Ag nanostructure substrate using the femtosecond laser for broad-band and tunable plasmonic enhancement," *ACS Nano*, vol. 6, pp. 5190–5197, Jun. 2012.
- [27] D. Acevedo *et al.*, "SERS active surface in two steps, patterning and metallization," *Adv. Eng. Mater.*, vol. 15, pp. 325–329, May 2013.
- [28] C. H. Lin *et al.*, "One-step fabrication of nanostructures by femtosecond laser for surface-enhanced Raman scattering," *Opt. Exp.*, vol. 17, pp. 21581–21589, Nov. 2009.
- [29] Z. B. Wang *et al.*, "Laser micro/nano fabrication in glass with tunable-focus particle lens array," *Opt. Exp.*, vol. 16, pp. 19706–19711, Nov. 2008.
- [30] S.M. Huang *et al.*, "Theoretical and experimental investigation of the near field under ordered silica spheres on substrate," *Appl. Phys. A*, vol. 96, pp. 459–466, Aug. 2009.
- [31] S. M. Huang *et al.*, "Nanobump arrays fabricated by laser irradiation of polystyrene particle layers on silicon," *Appl. Phys. Lett.*, vol. 86, Apr. 2005, Art. no. 161911.
- [32] A. Khan *et al.*, "Laser micro/nano patterning of hydrophobic surface by contact particle lens array," *Appl. Surf. Sci.*, vol. 258, pp. 774–779, Nov. 2011.
- [33] X. Sedao *et al.*, "Laser surface micro-/nano-structuring by a simple transportable micro-sphere lens array," *J. Appl. Phys.*, vol. 112, Nov. 2012, Art. no. 103111.
- [34] K. Piglmayer *et al.*, "Laser-induced surface patterning by means of microspheres," *Appl. Phys. Lett.*, vol. 80, Jun. 2002, Art. no. 4693.
- [35] A. Khan *et al.*, "Parallel near-field optical micro/nanopatterning on curved surfaces by transported micro-particle lens arrays," *J. Phys. D, Appl. Phys.*, vol. 43, Aug. 2010, Art. no. 305302.
- [36] S. M. Huang *et al.*, "Pulsed laser-assisted surface structuring with optical near-field enhanced effects," *J. Appl. Phys.*, vol. 92, pp. 2495–2500, Sep. 2002.
- [37] K. Leitz *et al.*, "Microsphere near-field nanostructuring using picosecond pulses," *Phys. Procedia*, vol. 5, pp. 237–244, Sep. 2010.
- [38] X. Sedao *et al.*, "Large area laser surface micro/nanopatterning by contact microsphere lens arrays," *Appl. Phys. A*, vol. 111, pp. 701–709, Jun. 2013.
- [39] C. Constantinescu *et al.*, "Laser processing of metal thin films using transparent microsphere arrays," *Appl. Surf. Sci.*, vol. 336, pp. 112–117, May 2015.
- [40] S. N. Agbo *et al.*, "Preferred crystal orientation in thin-film nanocrystalline silicon determined by Raman spectroscopy," *Dig. J. Nanomater. Biostruct.*, vol. 8, pp. 1461–1473, Oct. 2013.
- [41] Z. Papadopolos *et al.*, "Maximum density rule for bulk terminations of quasicrystals," *Phys. Rev. B*, vol. 69, Jun. 2004, Art. no. 224201.
- [42] E.C. Le Ru *et al.*, "Surface enhanced Raman scattering enhancement factors: A comprehensive study," *J. Phys. Chem. C*, vol. 111, pp. 13794–13803, Sep. 2007.
- [43] F. Zhang *et al.*, "Enhancement of Raman scattering by field superposition of rough submicrometer silver particles," *Appl. Phys. Lett.*, vol. 100, Apr. 2012, Art. no. 173103.